REDUCED GRAPHENE OXIDE AND Tb-DO3A CONJUGATE AS LUMINESCENT CHEMOSENSOR FOR AGILE DETECTION OF HYDROXYL RADICAL

Fatih ALGI*, Department of Biotechnology & ASUBTAM Memduh Bilmez BioNanoTech Lab., Aksaray University, TR-68100 Aksaray, TURKEY, falgi@aksaray.edu.tr
(https://orcid.org/0000-0001-9376-1770)
Meltem ALP, Department of Biotechnology & ASUBTAM Memduh Bilmez BioNanoTech Lab., Aksaray University, TR-68100 Aksaray, TURKEY, alpmeltemgr@gmail.com
(https://orcid.org/0000-0001-7383-3319)

Abstract

*The development of chemosensors for the detection of hydroxyl radicals (HO•) is a challenging task since HO• has an exceptionally short lifetime (in vivo half-life of ~1 ns). In this work, we have designed and synthesized a versatile probe, viz. **Tb@rGO**, for the detection of HO• amongst the biologically important ions and reactive oxygen species (ROS). Our design is based on covalent conjugation of reduced graphene oxide (rGO) with terbium (III)-1,4,7,10-tetraazacyclododecane-1,4,7-triacetic acid (Tb-DO3A). **Tb@rGO** is characterized by traditional spectroscopic methods including XRD, SEM, TEM, and zeta potential analysis. Furthermore, we elaborate the photophysical properties of **Tb@rGO**. Accordingly, our results attest that **Tb@rGO** has unique luminescence features, rendering it highly effective in the detection of HO•. Remarkably, **Tb@rGO** is highly selective to HO• among many biologically important species in 0.1 M pH 7.4 phosphate buffered saline solution. It is also noteworthy that the limit of detection (LOD) is 0.92 μM for HO•. Therefore, this novel material hold promises as selective turn-off luminescent HO• probe.*

Keywords: Terbium (III), Reduced graphene oxide, Reactive oxygen species, Hydroxyl radical, Luminescent probe

HİDROKSİL RADİKALİNİN HIZLI TESPİTİ İÇİN LÜMİNESANS KEMOSENSÖR OLARAK İNDİRGENMİŞ GRAFEN OKSİT VE Tb-DO3A KONJÜGATI

Özet

*Hidroksil radikallerinin (HO•) tespiti için kemosensörlerin geliştirilmesi, HO•'nun son derece kısa bir ömre sahip olması (in vivo yarılanma ömrü ~1 ns) nedeniyle zorlu bir iştir. Bu çalışmada biyolojik olarak önemli iyonlar ve reaktif oksijen türleri (ROS) arasında HO•'nun tespiti için kullanılabilecek çok yönlü bir prob **Tb@rGO** tasarladık ve sentezledik. Tasarımımız indirgenmiş grafen oksidin (rGO) terbiyum (III)-1,4,7,10-tetraazasiklododekan-1,4,7-triasetik asit (Tb-DO3A) ile kovalent konjugasyonuna dayanmaktadır. **Tb@rGO**, XRD, SEM, TEM ve zeta potansiyel analizini içeren geleneksel spektroskopik yöntemlerle karakterize edilmiştir. Ayrıca **Tb@rGO**'nun fotofiziksel özelliklerini de detaylandırdık. Buna göre, sonuçlarımız **Tb@rGO**'nun benzersiz lüminesans özelliklere sahip olduğunu ve bu özelliğin onu HO• tespitinde son derece etkili kıldığını doğrulamaktadır. Dikkat çekici bir şekilde **Tb@rGO** fosfat tamponlu salin (0,1 M PBS, pH 7,4) çözeltisinde biyolojik açıdan önemli birçok tür arasında HO•'ya karşı oldukça seçicidir. HO• için tespit sınırının (LOD) 0,92 μM olması da dikkat çekicidir. Bu nedenle, bu yeni malzeme, seçici lüminesans sönümlemeli HO• probu olarak umut vaat etmektedir.*

Anahtar Kelimeler: Terbiyum (III), İndirgenmiş grafen oksit, Reaktif oksijen türleri, Hidroksil radikali, Lüminesans prob

1. Introduction

Reactive oxygen species (ROS) can be classified in two groups as free radicals (hydroxyl, hydroperoxyl and superoxide radicals) and nonradical species (H_2O_2, HOCl, HOBr, and $^1O_2$) [1, 2]. They involve in various physiological processes such as immune function, mitogenic response, cellular signaling, protein phosphorylation and maintaining redox homeostasis [3–7]. However, high levels of ROS cause oxidative stress, which can lead to aging, inflammation and genesis or development of diseases by the destruction of

important biomolecules including nucleic acids, lipids, proteins, and carbohydrates [8]. In particular, deterioration of redox homeostasis is directly linked with several diseases including cardiovascular diseases, cancer, inflammation, diabetes mellitus, gastrointestinal and neurological diseases [9]. Besides, low levels of ROS are associated with autoimmune disorders [10]. Hydroxyl radical (HO•) is the most reactive ROS, and it has very short lifetime (in vivo half-life of ~1 ns). Moreover, the diffusion length of HO• (ca. 10^{-9} m) in aqueous solution is shorter than the other ROS [8, 11]. HO• is widely used in air quality monitoring and water purification [12]. Also, it is one of the reactive intermediates of photo and chemo dynamic cancer therapies. Furthermore, HO• has essential functions in the control of many pathological and physiological conditions. Therefore, real-time detection of HO• is significant to reveal the extent of its biological roles and functions as well as deleterious effects. Nonetheless, it is a challenge to get truly efficient chemosensors for HO• due to its transient nature.

Electron paramagnetic resonance (EPR) spectroscopy serves as a traditional method for the detection of HO•, but low spatiotemporal resolution and complex instrumentation limit its utility [8]. In this context, luminescence spectroscopy's practicality, selectivity, and sensitivity offer a potential approach to the precise identification of HO•. A number of organic fluorophores which can be used as chemosensors for HO• have been reported so far [12–16]. However, organic fluorophores [17–20] have some inherent drawbacks such as low photostability, broad luminescence peaks and small Stokes shifts [21]. On the contrary, lanthanide complexes represent a versatile platform for optical HO• chemosensors [21–29] due to their sufficient photostability, and sharp luminescence peaks in Visible or infra-red regions [30, 31]. Furthermore, lanthanide complexes also have large Stokes shifts (~200 nm), which eliminates self-absorption problems [27]. Additionally, lanthanide complexes allow time-delayed luminescence detection, eliminating any interference from background luminescence. Thus, these superior properties of lanthanide complexes have paved the way for numerous practical applications in different fields, including sensors [32–35], bioimaging agents [31, 36], and device applications [30, 37].

In the present work, we have created and synthesized a versatile probe to identify HO• amongst the ROS. Our design was based on covalent conjugation of terbium (III)-1,4,7,10-tetraazacyclododecane-1,4,7-triacetic acid (Tb-DO3A) with reduced graphene oxide (rGO) to get **Tb@rGO** (Figure 1). Here, we opted to use Tb(III) as the metal center for luminescence source and rGO as a robust antenna for the sensitization of the lanthanide luminescence [38–42]. **Tb@rGO** was characterized by traditional spectroscopic methods including XRD, SEM, TEM, and zeta potential analysis. Furthermore, we elaborated the photophysical properties of Tb@rGO. Accordingly, our results attested that **Tb@rGO** had

unique luminescence features, rendering it highly effective in the detection of HO•. Remarkably, **Tb@rGO** was highly selective to HO• amongst these ROS in aqueous solution at physiological pH (PBS, pH 7.4) solution. It was also noteworthy that the limit of detection (LOD) is 0.92 μM for HO•. Therefore, this novel material hold promises as an exceptionally selective and sensitive luminescent HO• probe.
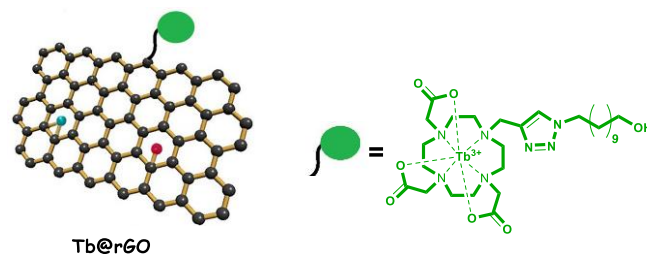

Figure 1. The structure of **Tb@rGO.**

2. Material and Method

Unless specified otherwise, chemicals were purchased from reliable commercial vendors and utilized exactly as supplied. Thermo Scientific Nicolet iS5 FT-IR Spectrometer with iD5-ATR and Perkin Elmer Spectrum 100 model FTIR with attenuated total reflectance (ATR) were used to record FTIR spectra, while Thermo Scientific TSQ Quantum Acces Max spectrometer was used to record LC-MS spectra. Varian Cary Eclipse and Varian Cary 50 spectrophotometers were used to record the fluorescence and UV-Vis measurements, respectively. The Merck Company's 60–200 mesh silica gel was used for column chromatography. Utilizing the Schorrp MPM-H2 model device, the melting points were ascertained. TLC was observed using analytical aluminum plates made of Merck with a 0.2 mm silica gel 60 F254. For each measurement, anions solutions made from the appropriate perchlorate salts were made freshly. Migros A.S., a local supplier, provided the hypochlorite solution (5% NaOCl). Using the methods outlined in the literature reactive oxygen species were prepared [43]. Varian Cary Eclipse spectrophotometers were used to measure phosphorescence in the range of 450 to 700 nm. The widths of the emission and excitation slits were 10 and 20 nm, respectively. The gate time and delay time were 2.00 and 0.10 ms, respectively, while the total decay time was 0.02 s and the number of flashes was 1.00. Voltage of the photomultiplier tube was high. Following slightly altered published protocols, the compound **3**, Tb-DO3A, were synthesized in four stages [35].

2.1. Synthesis of 11-azidoundecan-1-ol (2)

11-Bromo-1-undecanol (**1**, 251 mg, 1 mmol), sodium azide (98 mg, 1.5 mmol) and potassium iodide (16.6 mg, 0.1 mmol) were dissolved in 2 mL anhydrous DMF and placed in a 10 mL round-bottomed flask. The mixture was heated at 98 °C under argon atmosphere until compound **1** was exhausted and checked by TLC. The

solvent was extracted using less pressure after allowing the mixture to reach room temperature. DCM (3x100 mL) was used to extract the residue after it was put into 100 mL of water, and it was then dried over $MgSO_4$. Yellow viscose oil with a 70% yield was obtained by filtering the mixture and eliminating the solvent. ^1H NMR (300 MHz, $CDCl_3$) δ/ppm: 3.62 (t, J = 6.6 Hz, 3H), 3.23 (t, J = 6.6 Hz, 3H), 1.58 – 1.52 (m, 6H), 1.33 – 126 (m, 12H); ^{13}C NMR (75 MHz, $CDCl_3$) δ/ppm: 62.92, 51.44, 32.75, 29.49, 29.39, 29.36, 29.08, 28.78, 26.65, 25.70.

2.2. Synthesis of 4

3 (124.6 mg, 0.585 mmol) and **2** (0.585 mmol) were dissolved of in a mixture of THF and H_2O (1:1, v/v, 5 mL) under argon atmosphere. Cu dust (4 mg, 0.06 mmol) and $CuSO_4.5H2O$ (15 mg, 0.06 mmol) were added, and the mixture was stirred for 48 hours at room temperature in an argon environment. With the use of a rotary evaporator, the solvent was eliminated, yielding **4** in 75% yield, LC MS/MS (m/z) calculated M^+ for $C_{28}H_{48}N_7O_7Tb$: 753.29 measured $[M+H]^+$: 754.04, $[M+Na]^+$: 776.04.

2.3. Synthesis of Reduced Graphene Oxide

GO was synthesized by using a modified Hummer's method [44]. To begin with, 5 g of graphite was added to 115 mL of H_2SO_4 (98%) and 2.5 g $NaNO_3$ was allowed to mix in an ice bath for 30 minutes. $KMnO_4$ (15 g) was added to the mixture slowly and stirred for 3 h at 35 °C. Subsequently, 500 mL of water was slowly added, followed by stirring for 1 hour to maintain a temperature below 70°C. Gradually adding 10 mL of 30% H_2O_2 to the mixture caused the suspension's color to change from dark brown to yellow and caused vigorous bubbles to form. The solution was washed 3 times using dilute HCl (%10) followed by centrifuging at 5000 rpm for 10 minutes and then, to completely remove the acid, it was washed with distilled water until the pH was neutral. The filtrate was dried at 50 °C for 24 h to give graphite oxide. Graphite oxide (100 mg in 100 mL water) was ultrasonically sonicated for two hours to yield graphene oxide (GO). Then, GO was reduced by treatment with hydrazine hydrate (3 mL) at 115 °C for 2 h. The mixture was left to cool to room temperature once the reaction was finished, filtered, and washed with distilled water and methanol before drying under vacuum.

2.4. Synthesis of Tb@rGO

$SOCl_2$ (5 mL) was added dropwise to rGO (30 mg) solution in anhydrous DMF (0.5 mL) under argon atmosphere. The mixture was heated at 70 °C for 24 h and allowed to cool to room temperature. Unreacted $SOCl_2$ was removed by rotary evaporation under reduced pressure. Anhydrous DMF (0.5 mL) and NEt_3 (0.5 mL) and were added to the residue, followed by addition of **4** (0.04 mmol) in anhydrous DMF. In under argon atmosphere, the mixture was heated to 85 °C. After 48 h, allowing the mixture to reach room temperature, a saturated $NaHCO_3$ solution was used to wash it. The supernatant was centrifuged at 25 °C for 5 minutes at 12000 rpm. The pellet was washed with distilled water and methanol, before drying under vacuum.

2.5. Detection Limit Measurements

The detection limit for **Tb@rGO** was calculated based on luminescence titration. Figure S12 illustrates the luminescence emission intensity of **Tb@rGO** with the concentration of •OH. Firstly, determine the S/N ratio, the phosphorescence emission intensity of the blanks without •OH was measured 10 times. After that standard deviation of these blanks was calculated. Phosphorescence emission intensities of the **Tb@rGO** in the presence of ·OH was plotted as a concentration of ·OH to determine the slopes. In general, Stern-Volmer plot is used for luminescence quenching [45]. We used an exponential quenching equation (1) to fit the nonlinear Stern-Volmer curve [45–48]. The concentration of ·OH can be placed as a function of equation (1), where I_0 and I are the emission intensity of the suspension without or with the addition of ·OH, respectively.

$$(I_0/I) = 1.0479e^{6650(•OH)} \quad (1)$$

The result illustrates that the plot can be fitted to (I_0/I) = 1.0479 $e^{6650(•OH)}$ and attains the correlation coefficient (R^2) of 0.991 (see Figure S12). We calculated the quenching constant for ·OH from this non-linear curve fitting as 71259.07. Equation $(3σ/m)$ was used to get the detection limit, where σ shows the standard deviation of the blank measurements, m illustrates the slope between sample concentration towards intensity. Standard deviation was determined as 0.021963042 and the slope of the graph as 71259.07, thus in turn, the limit of detection (LOD) was calculated in line with the equation (0.92 µM). The limit of quantification (LOQ) was calculated according to the equation $(10σ/m)$ as 3.08 µM. Remarkably, Table S6 shows that **Tb@rGO's** LOD for •OH remains comparable to, superior to other luminescent probes reported in the literature.

3.   Results and Discussion

3.1. Synthesis and and characterization of Tb@rGO

The target chemical **Tb@rGO** was synthesized by first converting 11-Bromo-1-undecanol (**1**) to 11-azidoundecan-1-ol (**2**) by treatment with sodium azide in the presence of potassium iodide in DMF (Scheme 1). Compound **2** was characterized with ^1H, ^{13}C NMR and FTIR spectra (see Supporting Information, Figure S1-S3). Tb(III)-DO3A (**3**) was synthesized according to literature [35]. Cu-catalyzed click reaction between **2** and **3** provided compound **4** in 75% yield (Scheme 1). Compound **4** was characterized by LC MS and FTIR spectra (Figure S4-S7).
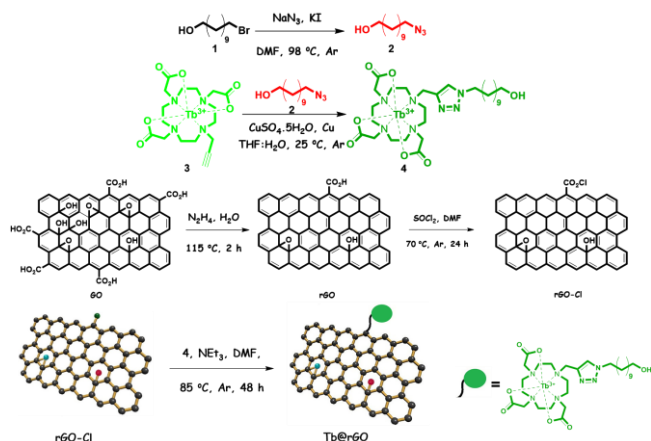
Figure 2. Synthesis of **2**, **4**, rGO-Cl, and **Tb@rGO**.

Using the Modified Hummer method, Graphene oxide (GO) was synthesized (Figure 2)[44]. The reduction of GO was carried out with hydrazine at 115 °C (for the details of characterization of GO and rGO, see Supporting Information, Figure S8-S12). The treatment of rGO with $SOCl_2$ in dry DMF at 70 °C afforded rGO-Cl. rGO-Cl was directly used in the next step, and it was treated with compound **4** in the presence of NEt_3 in dry DMF to furnish **Tb@rGO** (Scheme 1). **Tb@rGO** was characterized by SEM, TEM, XRD, zeta potential, and EDX analysis (see Figures 3-6).

Figure 3 shows TEM and SEM images of rGO and **rGO@Tb**. Compared to GO, rGO has a smoother surface because functional groups are removed following reduction (see Figure 3a, and Figure S8). However, the rGO's surface morphology was dramatically changed after reaction of rGO-Cl with **4**. The flocculent morphology clearly indicated that **4** was successfully conjugated to rGO to furnish **rGO@**Tb (Figure 3a-d). Figure 3c-d shows TEM images of rGO and **rGO@Tb**. It was seen that there was a defect in the **rGO@Tb** structure. With the removal of oxygen-containing groups, defects occurred in the structure of the basal plane (Figure 3d) [49]. A flat morphology with reduced folding and wrinkling was also observed. The appearance of many dark spots on the rGO sheets unambiguously indicated the conjugation of **4** to provide **rGO@Tb** [41, 50].
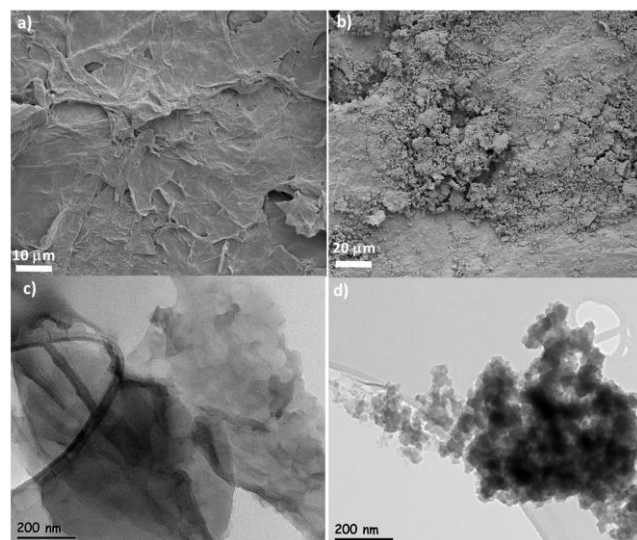

Figure 3. SEM images of **a)** rGO, **b)** Tb@rGO, and TEM images **c)** rGO, **d) Tb@rGO**.

XRD patterns of GO, rGO, and **Tb@rGO** is demonstrated in Figure 4. As seen in Figure 4, characteristic reflection plane (001) of GO (at the diffraction peak 2θ=11.54°) disappeared after reduction with hydrazine and the reflection plane (002) at 2θ=26.8° appeared in XRD spectrum [44, 51, 52]. Furthermore, **Tb@rGO** exhibited a characteristic peak appeared at 30.3°. The average number of layers (n) and crystallite size (D) for GO, rGO and **Tb@rGO** were determined according to literature [53–55], and the results were tabulated in Table S1. After reducing GO to rGO, the peak shifted from 11.54° to 26.8°, which confirmed the reduction of inter-layer spacing to 3.91 Å for rGO due to the regeneration of sp^2 domains and the removal of oxygen-rich functionalities. Table S1 shows that average number of layers (n) significantly decreased upon reduction, from n=21 for GO to n=3 for rGO and **Tb@rGO**, respectively. Overall, XRD data proved that of Tb(III) macrocycle was successfully attached to rGO [56, 57].
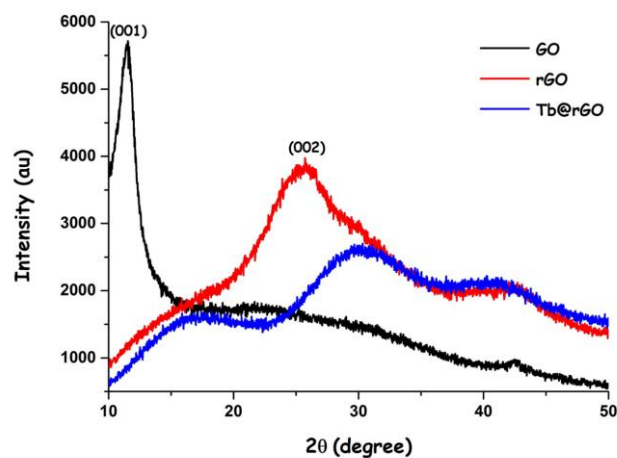

Figure 4. XRD patterns of GO, rGO, and Tb@rGO.

One important metric for assessing the stability of colloidal dispersion is zeta potential [58, 59]. The surface charge of the GO, rGO, and **Tb@rGO** was determined by the zeta potential measurements in 0.1 M pH 7.4 PBS solution. The zeta potential of GO and rGO were determined as -34.3 mV and -42.9 mV, respectively (Figure S11-S12) [60]. However, the successful attachment of Tb(III) macrocycle to rGO raised the zeta potential of **Tb@rGO** up to -33.0 mV under the same conditions (Figure 5).
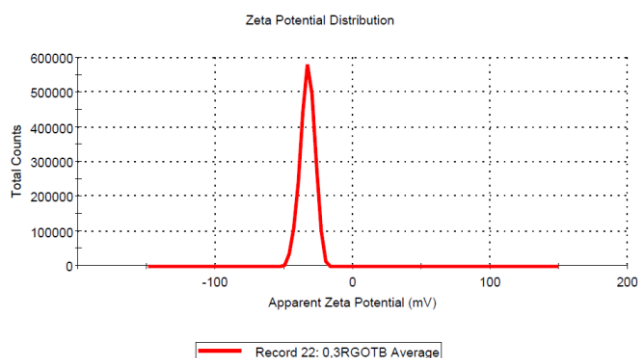

Figure 5. Zeta potential of **Tb@rGO** in PBS (0.1 M PBS; pH 7.4; -33.0).

Furthermore, EDX spectroscopy was utilized to divulge the components of the GO, rGO, and **Tb@rGO**, all of which were expected to have different C:O ratios [61, 62]. Table S2 summarizes the results of EDX analysis and C:O ratios for GO, rGO, and **Tb@rGO**. Apparently, the reduction of GO to rGO resulted in an increased C:O ratio owing to the reduction of oxygenated functional groups. However, we found that C:O ratio of **Tb@rGO** was around 3.25, which could be due to the formation of some defects in the structure. EDX analyzes of GO, rGO, and **Tb@rGO** are given in Tables S3-S5 and Figure S9-S10, respectively. EDX analysis of **Tb@rGO** unambiguously show the presence of Tb in the structure, thus confirming the covalent conjugation of **4** to rGO to provide **Tb@rGO** (Figure 6).
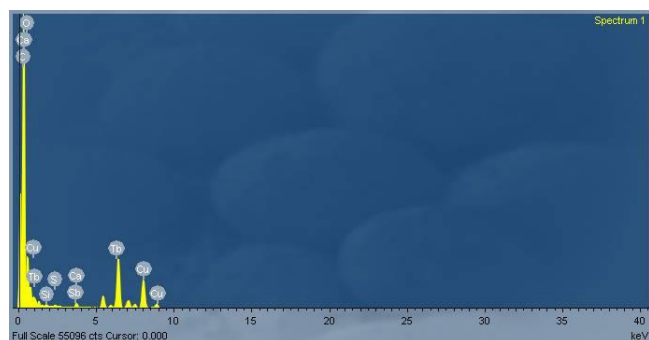

Figure 6. EDX analysis of **Tb@rGO.**

3.2. Photophysical properties and sensing features of Tb@rGO features of Tb@rGO

UV-Vis absorption spectra of GO, and rGO represent the absorption peak at 235 nm and 275 nm in 0.1 M pH 7.4

PBS, respectively. The strong absorption peak at 235 nm in the UV–vis spectrum of GO corresponds to $\pi-\pi^*$ transitions, which was shifted to 275 nm after reduction of GO to reduced graphene oxide [51, 63]. Photophysical properties of **Tb@rGO** were investigated in PBS solution (0.1 M, pH 7.4). The phosphorescence emission spectrum of **Tb@rGO** (16 μg/mL) was characterized emission peak with a λ_{em} at 544 nm when excited at 275 nm (Figure 7). Phosphorescence spectra of rGO, **4**, and **Tb@rGO** in PBS solution upon excitation at 275 nm were given in Figure S13. rGO had a weak emission band between 525 nm to 585 nm. On the other hand, **4** and **Tb@rGO** exhibited similar characteristics of Tb(III) emission between 450 nm and 650 nm, albeit the phosphorescence emission intensity of **Tb@rGO** was slightly declined when compared to **4** under the same conditions. Unambiguously, the phosphorescence spectra proved that Tb(III) macrocycle was successfully attached to rGO to give **Tb@rGO**. Next, the consequenceo of pH on the phosphorescence emission of **Tb@rGO** was examined between pH 5 and pH 9. It was observed that phosphorescence emission of **Tb@rGO** was unaffected by pH (Figure 7).
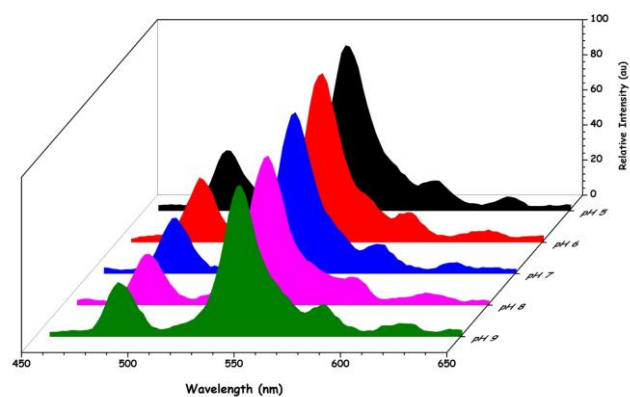

Figure 7. Consequence of pH on the phosphorescence spectrum of **Tb@rGO** (16 μg/mL) in 0.1 M pH 7.4 PBS at room temperature (λ_{em}=544 nm, λ_{ex}=275 nm).

Using various analytes, spectrophotometric titrations were carried out to examine the analyte responsiveness of **Tb@rGO** in the same solution. Here, biologically important ions including Cl^-, HSO_4^-, F^-, Br^-, I^-, PO_4^{3-}, HPO_4^{2-}, $H_2PO_4^-$, NO_2^-, SO_4^{2-}, SH^-, BF_4^-, CO_3^{2-}, S^{2-}, IO_3^-, N_3^-, HCO_3^-, OH^-, NO_3^-, CN^-, OAc^-, citrate, along with some reactive oxygen species such as ClO^-, O_2^-, H_2O_2, and $^1O_2$ were tested (6.5×10^{-5} M). For the selectivity experiment, O_2^- and hypochlorite (ClO^-) anions were prepared from commercial KO_2 (dissolved in DMSO) and NaClO. Fresh H_2O_2 solution (30%, v/v) was made using commercial H_2O_2. NaClO solution reacted with hydrogen peroxide (H_2O_2) to was produce singlet oxygen ($^1O_2$). Figure 8 depicts the relative phosphorescence emission intensity of **Tb@rGO** (16 μg/mL) in the presence of various analytes (Cl^-, HSO_4^-, Br^-, PO_4^{3-}, F^-, I^-, HPO_4^{2-}, $H_2PO_4^-$, NO_2^-, SO_4^{2-}, SH^-, BF_4^-, CO_3^{2-}, S^{2-}, IO_3^-, N_3^-, HCO_3^-, OH^-, NO_3^-, CN^-,

OAc$^-$, citrate, ClO$^-$, O$_2^-$, H$_2$O$_2$, ^{1}O$_2$, O$_2^-$, $\cdot$OH) in 0.1 M pH 7.4 PBS (λ_{em}=544 nm, λ_{ex}=275 nm) at room temperature. There was no notable alteration in the emission spectra of **Tb@rGO** caused by any of these species. However, the emission intensity of **Tb@rGO** decreased dramatically when $\cdot$OH was generated *in situ* from H$_2$O$_2$ in the presence of Fe(II) via Fenton reaction (Figure 8). Fenton reaction is suitable for quantitative analysis of HO$\cdot$. Therefore, differing ratios of Fe^{2+} and H$_2$O$_2$ (1:10) was produced HO$\cdot$ through the Fenton reaction. Note that there was no change in the emission intensity upon addition of H$_2$O$_2$ or Fe^{2+} alone. This result indicated that the probe was unable to react with either H$_2$O$_2$ or Fe^{2+}. However, the solution's luminescence intensity was greatly reduced when H$_2$O$_2$ and Fe^{2+} were combined. Apparently, **Tb@rGO** is an extremely selective and specific luminescent probe for the identification of HO$\cdot$ (Figure 9) [21].
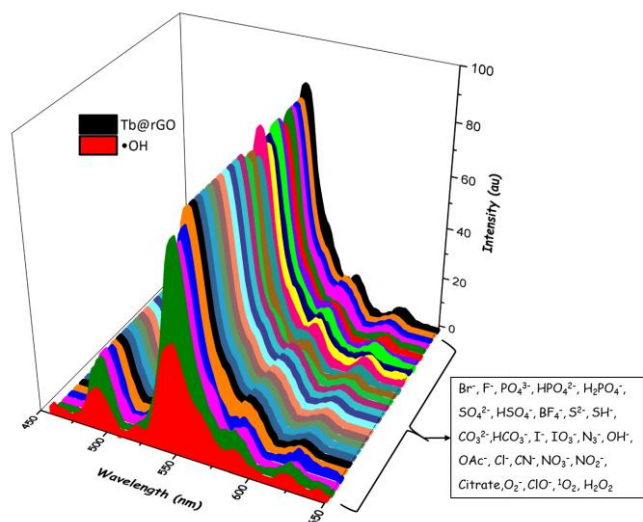

Figure 8. Phosphorescence spectrum of **Tb@rGO** (16 μg/mL) in the presence of various analytes (6.5x10^{-5} M, F$^-$, Cl$^-$, HSO$_4^-$, Br$^-$, I$^-$, PO$_4^{3-}$, HPO$_4^{2-}$, H$_2$PO$_4^-$, NO$_2^-$, SO$_4^{2-}$, SH$^-$, BF$_4^-$, CO$_3^{2-}$, S^{2-}, IO$_3^-$, N$_3^-$, HCO$_3^-$, OH$^-$, NO$_3^-$, CN$^-$, OAc$^-$, citrate, ClO$^-$, O$_2^-$, H$_2$O$_2$, ^{1}O$_2$, O$_2^-$, and $\cdot$OH) in 0.1 M pH 7.4 PBS (λ_{em}=544 nm, λ_{ex}=275 nm) at room temperature.
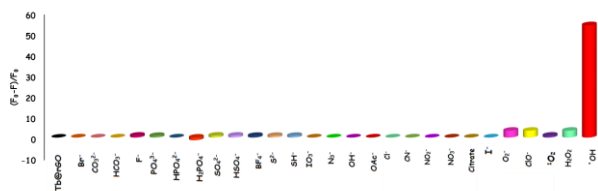

Figure 9. Relative phosphorescence emission intensity of **Tb@rGO** (16 μg/mL) in the presence of various analytes (6.5x10^{-5} M, F$^-$, Cl$^-$, HSO$_4^-$, Br$^-$, I$^-$, PO$_4^{3-}$, HPO$_4^{2-}$, H$_2$PO$_4^-$, NO$_2^-$, SO$_4^{2-}$, SH$^-$, BF$_4^-$, CO$_3^{2-}$, S^{2-}, IO$_3^-$, N$_3^-$, HCO$_3^-$, OH$^-$, NO$_3^-$, CN$^-$, OAc$^-$, citrate, ClO$^-$, O$_2^-$, H$_2$O$_2$, ^{1}O$_2$ O$_2^-$, and $\cdot$OH) in PBS (0.1 M, pH 7.4; λ_{em}=544 nm, λ_{ex}=275 nm) at room temperature.

The effect of HO$\cdot$ concentration on the emission of **Tb@rGO** was examined in detail. The luminescence response of **Tb@rGO** to HO$\cdot$ was correlated with H$_2$O$_2$ concentration. Figure 10 shows the phosphorescence spectral changes of **Tb@rGO** as a function of $\cdot$OH concentration (from 9x10^{-5} M to 1.9x10^{-3} M) in 0.1 M pH 7.4 PBS at room temperature. When HO$\cdot$ was added, the phosphorescence emission of **Tb@rGO** was turned off, leading to an around 12-fold decrease in emission intensity (Figure 10). The quenching efficiency was 91.7%.
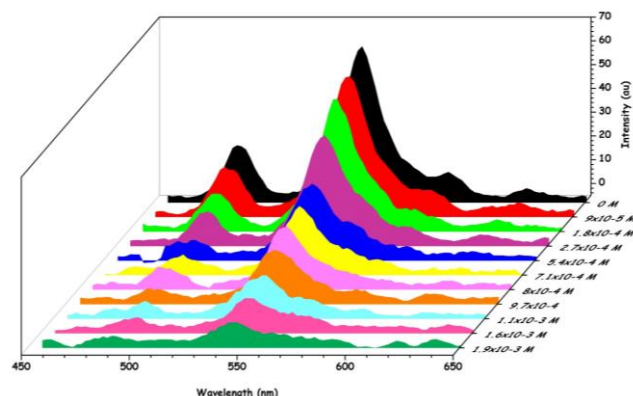

Figure 10. Phosphorescence emission spectra of **Tb@rGO** (16 μg/mL) as a function of various concentration of HO$\cdot$ (from 9x10^{-5} M to 1.9x10^{-3} M) in 0.1 M pH 7.4 PBS (λ_{em}=544 nm, λ_{ex}=275 nm) at room temperature.

Figure 11 illustrates that the phosphorescence emission intensity of **Tb@rGO** varies significantly depending on the concentration of HO$\cdot$. Based on the above spectrophotometric titrations, limit of detection (LOD) of **Tb@rGO** for HO$\cdot$ was determined to be 9.2x10^{-7} M (Figure S14). Figure 11 shows that the phosphorescence emission intensity of **Tb@rGO** (16 μg/mL) did not cause a substantial change even in the presence of the analyte mixture (see black and red graphs). In contrast, emission intensity of **Tb@rGO** sharply decreased when HO$\cdot$ was added in the presence of analyte mixture in 0.1 M pH 7.4 PBS (λ_{em}=544 nm, λ_{ex}=275 nm) at room temperature. Gratifyingly, these results revealed that the probe possesses high selectivity and sensitivity toward HO$\cdot$ even in the presence of many other species. Remarkably, the response of **Tb@rGO** for HO$\cdot$ was unaffected by the backdrop of different species.
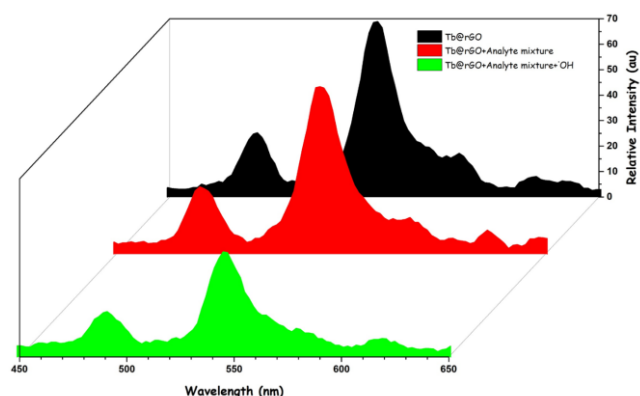
Figure 11. Phosphorescence emission spectra of **Tb@rGO** (16 μg/mL) in the presence of analyte mixture (F^-, Cl^-, HSO_4^-, Br^-, I^-, PO_4^{3-}, HPO_4^{2-}, $H_2PO_4^-$, NO_2^-, SO_4^{2-}, SH^-, BF_4^-, CO_3^{2-}, S^{2-}, IO_3^-, N_3^-, HCO_3^-, OH^-, NO_3^-, CN^-, OAc^-, citrate, ClO^-, O_2^-, H_2O_2, $^1O_2$ O_2^-) in 0.1 M pH 7.4 PBS (λ_{em}=544 nm, λ_{ex}=275 nm) at room temperature.

Finally, we investigated the luminescence response of the constituents of **Tb@rGO** (**4** and rGO) to ROS under the same conditions. It was noteworthy that **4** was responsive to both HO• and ClO^-, indicating that **4** did not induce selectivity to HO• (Figure 12). On the other hand, rGO was almost nonresponsive to these ROS (Figure S15).
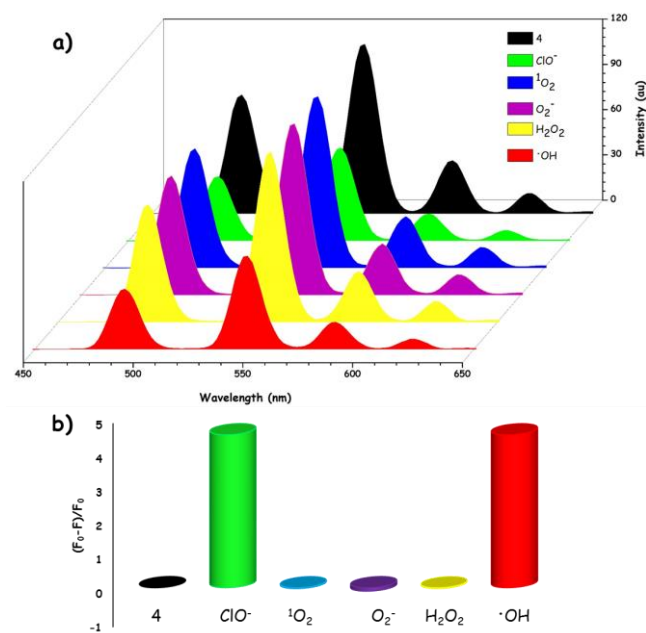

Figure 12. a) Phosphorescence emission spectra, and b) Relative emission intensity of **4** in the presence of ROS in 0.1 M pH 7.4 PBS at room temperature (λ_{em}=544 nm, λ_{ex}=275 nm).

4.   Conclusions

In summary, we investigated the phosphorescence characteristics, synthesis, and design of a unique material, **Tb@rGO**. We successfully demonstrated that

Tb@rGO could be used as phosphorescent HO• probe. Remarkably, **Tb@rGO** is highly selective to HO• amongst the biologically important species and ROS in PBS solution. Depending on the concentration of HO•, the intensity of the phosphorescence emission varied markedly, which allowed quantitative detection of HO•. On that basis, LOD and the limit of quantification were found to be 0.92 μM and 3.08 μM, respectively. Therefore, this novel material hold promises as selective turn-off luminescent HO• probe.

6.   References

[1]   X. Bai, K. K.-H. Ng, J. J. Hu, S. Ye, and D. Yang, "Small-molecule-based fluorescent sensors for selective detection of reactive oxygen species in biological systems," *Annu. Rev. Biochem.*, vol. 88, pp. 605–633, 2019.

[2]   T. D. Pollard and B. O'Shaughnessy, "Molecular mechanism of cytokinesis," *Annu. Rev. Biochem.*, vol. 88, pp. 661–689, 2019.

[3]   Y. Geng, Z. Wang, J. Zhou, M. Zhu, J. Liu, and T. D. James, "Recent progress in the development of fluorescent probes for imaging pathological oxidative stress," *Chem. Soc. Rev.*, vol. 52, no. 11, pp. 3873–3926, 2023, doi: 10.1039/D2CS00172A.

[4]   S. K. Kailasa, G. N. Vajubhai, J. R. Koduru, and T. J. Park, "Recent progress of nanomaterials for colorimetric and fluorescence sensing of reactive oxygen species in biological and environmental samples," *Trends Environ. Anal. Chem.*, vol. 37, p. e00196, 2023, doi: https://doi.org/10.1016/j.teac.2023.e00196.

[5]   H.-S. Wang, "Development of fluorescent and luminescent probes for reactive oxygen species," *TrAC Trends Anal. Chem.*, vol. 85, pp. 181–202, 2016.

[6]   N. Kwon, D. Kim, K. M. K. Swamy, and J. Yoon, "Metal-coordinated fluorescent and luminescent probes for reactive oxygen species (ROS) and reactive nitrogen species (RNS)," *Coord. Chem. Rev.*, vol. 427, p. 213581, 2021, doi: https://doi.org/10.1016/j.ccr.2020.213581.

[7]   H. Sies *et al.*, "Defining roles of specific reactive oxygen species (ROS) in cell biology and physiology," *Nat. Rev. Mol. Cell Biol.*, vol. 23, no. 7, pp. 499–515, 2022, doi: 10.1038/s41580-022-

00456-z.

[8]   Y. You and W. Nam, "Designing photoluminescent molecular probes for singlet oxygen, hydroxyl radical, and iron–oxygen species," *Chem. Sci.*, vol. 5, no. 11, pp. 4123–4135, 2014.

[9]   X. Jiao, Y. Li, J. Niu, X. Xie, X. Wang, and B. Tang, "Small-molecule fluorescent probes for imaging and detection of reactive oxygen, nitrogen, and sulfur species in biological systems," *Anal. Chem.*, vol. 90, no. 1, pp. 533–555, 2018.

[10]   E. Sassetti, M. H. Clausen, and L. Laraia, "Small-molecule inhibitors of reactive oxygen species production," *J. Med. Chem.*, vol. 64, no. 9, pp. 5252–5275, 2021.

[11]   S. Ding, M. Li, H. Gong, Q. Zhu, G. Shi, and A. Zhu, "Sensitive and selective measurement of hydroxyl radicals at subcellular level with tungsten nanoelectrodes," *Anal. Chem.*, vol. 92, no. 3, pp. 2543–2549, 2020.

[12]   X. Qu, Y. Bian, Y. Chen, and X. Wei, "A sensitive BODIPY-based fluorescent probe for detecting endogenous hydroxyl radicals in living cells," *RSC Adv.*, vol. 10, no. 48, pp. 28705–28710, 2020.

[13]   X. Qu, W. Song, and Z. Shen, "A highly selective NIR fluorescent turn-on probe for hydroxyl radical and its application in living cell images," *Front. Chem.*, vol. 7, p. 598, 2019.

[14]   Y. Zhao, H. Li, Z. Chai, W. Shi, X. Li, and H. Ma, "An endoplasmic reticulum-targeting fluorescent probe for imaging· OH in living cells," *Chem. Commun.*, vol. 56, no. 47, pp. 6344–6347, 2020.

[15]   L. Chen *et al.*, "An edaravone-guided design of a rhodamine-based turn-on fluorescent probe for detecting hydroxyl radicals in living systems," *Anal. Chem.*, vol. 93, no. 42, pp. 14343–14350, 2021.

[16]   Y. Wu *et al.*, "Synthesis of dihydroquinolines as scaffolds for fluorescence sensing of hydroxyl radical," *Org. Lett.*, vol. 23, no. 1, pp. 135–139, 2020.

[17]   A. Degirmenci and F. Algi, "Synthesis, chemiluminescence and energy transfer efficiency of 2, 3-dihydrophthalazine-1, 4-dione and BODIPY dyad," *Dye. Pigment.*, vol. 140, pp. 92–99, 2017.

[18]   S. Karakaya and F. Algi, "A novel dual channel responsive zinc (II) probe," *Tetrahedron Lett.*, vol. 55, no. 40, pp. 5555–5559, 2014.

[19]   M. Pamuk and F. Algi, "Incorporation of a 2, 3-dihydro-1H-pyrrolo [3, 4-d] pyridazine-1, 4 (6H)-dione unit into a donor–acceptor triad: synthesis and ion recognition features," *Tetrahedron Lett.*, vol. 53, no. 52, pp. 7117–7120, 2012.

[20]   A. Degirmenci, D. Iskenderkaptanoglu, and F. Algi, "A novel turn-off fluorescent Pb (II) probe based on 2, 5-di (thien-2-yl) pyrrole with a pendant crown ether," *Tetrahedron Lett.*, vol. 56,

no. 4, pp. 602–607, 2015.

[21]   G. Cui, Z. Ye, J. Chen, G. Wang, and J. Yuan, "Development of a novel terbium (III) chelate-based luminescent probe for highly sensitive time-resolved luminescence detection of hydroxyl radical," *Talanta*, vol. 84, no. 3, pp. 971–976, 2011.

[22]   F. Ahmed, M. Muzammal Hussain, W. Ullah Khan, and H. Xiong, "Exploring recent advancements and future prospects on coordination self-assembly of the regulated lanthanide-doped luminescent supramolecular hydrogels," *Coord. Chem. Rev.*, vol. 499, p. 215486, 2024, doi: https://doi.org/10.1016/j.ccr.2023.215486.

[23]   R. Sivakumar and N. Y. Lee, "Recent advances in luminescent lanthanides and transition metal complex-based probes for imaging reactive oxygen, nitrogen, and sulfur species in living cells," *Coord. Chem. Rev.*, vol. 501, p. 215563, 2024, doi: https://doi.org/10.1016/j.ccr.2023.215563.

[24]   C. Galaup, C. Picard, F. Couderc, V. Gilard, and F. Collin, "Luminescent lanthanide complexes for reactive oxygen species biosensing and possible application in Alzheimer's diseases," *FEBS J.*, vol. 289, no. 9, pp. 2516–2539, May 2022, doi: https://doi.org/10.1111/febs.15859.

[25]   S. E. Page, K. T. Wilke, and V. C. Pierre, "Sensitive and selective time-gated luminescence detection of hydroxyl radical in water," *Chem. Commun.*, vol. 46, no. 14, pp. 2423–2425, 2010.

[26]   Y. Xiao, Z. Ye, G. Wang, and J. Yuan, "A ratiometric luminescence probe for highly reactive oxygen species based on lanthanide complexes," *Inorg. Chem.*, vol. 51, no. 5, pp. 2940–2946, 2012.

[27]   K. L. Peterson, M. J. Margherio, P. Doan, K. T. Wilke, and V. C. Pierre, "Basis for sensitive and selective time-delayed luminescence detection of hydroxyl radical by lanthanide complexes," *Inorg. Chem.*, vol. 52, no. 16, pp. 9390–9398, 2013.

[28]   J. Gao, Q. Li, C. Wang, and H. Tan, "Ratiometric detection of hydroxy radicals based on functionalized europium (III) coordination polymers," *Microchim. Acta*, vol. 185, pp. 1–8, 2018.

[29]   D. M. D. Leguerrier, R. Barré, J. K. Molloy, and F. Thomas, "Lanthanide complexes as redox and ROS/RNS probes: A new paradigm that makes use of redox-reactive and redox non-innocent ligands," *Coord. Chem. Rev.*, vol. 446, p. 214133, 2021.

[30]   S.-Y. Wu, X.-Q. Guo, L.-P. Zhou, and Q.-F. Sun, "Fine-tuned visible and near-infrared luminescence on self-assembled lanthanide-organic tetrahedral cages with triazole-based chelates," *Inorg. Chem.*, vol. 58, no. 10, pp. 7091–7098, 2019.

[31] M. C. Heffern, L. M. Matosziuk, and T. J. Meade, "Lanthanide probes for bioresponsive imaging," *Chem. Rev.*, vol. 114, no. 8, pp. 4496–4539, 2014.

[32] L. Xu *et al.*, "Continuously tunable nucleotide/lanthanide coordination nanoparticles for DNA adsorption and sensing," *ACS omega*, vol. 3, no. 8, pp. 9043–9051, 2018.

[33] M. Bilmez, A. Degirmenci, M. P. Algi, and F. Algi, "A phosphorescent fluoride probe based on Eu (III)-DO3A clicked with a 2, 5-di (thien-2-yl) pyrrole scaffold," *New J. Chem.*, vol. 42, no. 1, pp. 450–457, 2018.

[34] M. Alp, M. Pamuk Algi, and F. Algi, "Eu(III)–DO3A and BODIPY dyad as a chemosensor for anthrax biomarker," *Luminescence*, 2021, doi: 10.1002/BIO.4129.

[35] M. Alp, M. P. Algi, and F. Algi, "Tb (III)-DO3A and BODIPY dyad as multimode responsive hypochlorite probe," *Spectrochim. Acta Part A Mol. Biomol. Spectrosc.*, vol. 264, p. 120310, 2022.

[36] J.-C. G. Bünzli, "Lanthanide light for biology and medical diagnosis," *J. Lumin.*, vol. 170, pp. 866–878, 2016.

[37] Q. Zhang, S. O'Brien, and J. Grimm, "Biomedical applications of lanthanide nanomaterials, for imaging, sensing and therapy," *Nanotheranostics*, vol. 6, no. 2, p. 184, 2022.

[38] F. R. Baptista, S. A. Belhout, S. Giordani, and S. J. Quinn, "Recent developments in carbon nanomaterial sensors," *Chem. Soc. Rev.*, vol. 44, no. 13, pp. 4433–4453, 2015.

[39] C. Chien *et al.*, "Tunable photoluminescence from graphene oxide," *Angew. Chemie Int. Ed.*, vol. 51, no. 27, pp. 6662–6666, 2012.

[40] S. Pang, Z. Zhou, and Q. Wang, "Terbium-containing graphene oxide and its opto-electrochemical response for hypochlorite in water," *Carbon N. Y.*, vol. 58, pp. 232–237, 2013.

[41] Z. Zhou and Q. Wang, "An efficient optical-electrochemical dual probe for highly sensitive recognition of dopamine based on terbium complex functionalized reduced graphene oxide," *Nanoscale*, vol. 6, no. 9, pp. 4583–4587, 2014.

[42] B. Liu *et al.*, "From graphite to graphene oxide and graphene oxide quantum dots," *Small*, vol. 13, no. 18, p. 1601001, 2017.

[43] A. Degirmenci, O. Sonkaya, C. Soylukan, T. Karaduman, and F. Algi, "BODIPY and 2, 3-Dihydrophthalazine-1, 4-Dione Conjugates As Heavy Atom-Free Chemiluminogenic Photosensitizers," *ACS Appl. Bio Mater.*, 2021.

[44] L. Shahriary and A. A. Athawale, "Graphene oxide synthesized by using modified hummers approach," *Int. J. Renew. Energy Environ. Eng*, vol. 2, no. 01, pp. 58–63, 2014.

[45] J. Han, X. Bu, D. Zhou, H. Zhang, and B. Yang, "Discriminating Cr (III) and Cr (VI) using aqueous CdTe quantum dots with various surface ligands," *RSC Adv.*, vol. 4, no. 62, pp. 32946–32952, 2014.

[46] D. Dinda, A. Gupta, B. K. Shaw, S. Sadhu, and S. K. Saha, "Highly selective detection of trinitrophenol by luminescent functionalized reduced graphene oxide through FRET mechanism," *ACS Appl. Mater. Interfaces*, vol. 6, no. 13, pp. 10722–10728, 2014.

[47] W. Wei, R. Lu, S. Tang, and X. Liu, "Highly cross-linked fluorescent poly (cyclotriphosphazene-co-curcumin) microspheres for the selective detection of picric acid in solution phase," *J. Mater. Chem. A*, vol. 3, no. 8, pp. 4604–4611, 2015.

[48] J. Liu *et al.*, "A superamplification effect in the detection of explosives by a fluorescent hyperbranched poly (silylenephenylene) with aggregation-enhanced emission characteristics," *Polym. Chem.*, vol. 1, no. 4, pp. 426–429, 2010.

[49] N. G. de Barros *et al.*, "Graphene Oxide: A Comparison of Reduction Methods," *C*, vol. 9, no. 3, p. 73, 2023.

[50] J. Jiao, M. Pan, X. Liu, B. Li, J. Liu, and Q. Chen, "A non-enzymatic sensor based on trimetallic nanoalloy with poly (diallyldimethylammonium chloride)-capped reduced graphene oxide for dynamic monitoring hydrogen peroxide production by cancerous cells," *Sensors*, vol. 20, no. 1, p. 71, 2019.

[51] H. Saleem, M. Haneef, and H. Y. Abbasi, "Synthesis route of reduced graphene oxide via thermal reduction of chemically exfoliated graphene oxide," *Mater. Chem. Phys.*, vol. 204, pp. 1–7, 2018.

[52] D. Konios, M. M. Stylianakis, E. Stratakis, and E. Kymakis, "Dispersion behaviour of graphene oxide and reduced graphene oxide," *J. Colloid Interface Sci.*, vol. 430, pp. 108–112, 2014.

[53] U. Holzwarth and N. Gibson, "The Scherrer equation versus the'Debye-Scherrer equation'," *Nat. Nanotechnol.*, vol. 6, no. 9, p. 534, 2011.

[54] P. Saini, R. Sharma, and N. Chadha, "Determination of defect density, crystallite size and number of graphene layers in graphene analogues using X-ray diffraction and Raman spectroscopy," *Indian J. Pure Appl. Phys.*, vol. 55, no. 9, pp. 625–629, 2017.

[55] P. W. Albers, V. Leich, A. J. Ramirez-Cuesta, Y. Cheng, J. Hönig, and S. F. Parker, "The characterisation of commercial 2D carbons: graphene, graphene oxide and reduced graphene oxide," *Mater. Adv.*, vol. 3, no. 6, pp. 2810–2826, 2022.

[56] C. Jiao, R. Zhong, Y. Zhou, and H. Zhang, "Preparation and Characterization of a Novel Terbium Complex Coordinated with 10-Undecenoic Acid for UV-Cured Coatings," *Int. J. Polym. Sci.*, vol. 2020, 2020.

[57] E. Montes *et al.*, "Effect of pH on the optical and structural properties of HfO2: Ln3+, synthesized by hydrothermal route," *J. Lumin.*, vol. 175, pp. 243–248, 2016.

[58] B. Konkena and S. Vasudevan, "Understanding aqueous dispersibility of graphene oxide and reduced graphene oxide through p K a measurements," *J. Phys. Chem. Lett.*, vol. 3, no. 7, pp. 867–872, 2012.

[59] S. Lee, S. Bong, J. Ha, M. Kwak, S.-K. Park, and Y. Piao, "Electrochemical deposition of bismuth on activated graphene-nafion composite for anodic stripping voltammetric determination of trace heavy metals," *Sensors Actuators B Chem.*, vol. 215, pp. 62–69, 2015.

[60] T. A. Tabish *et al.*, "In vitro toxic effects of reduced graphene oxide nanosheets on lung cancer cells," *Nanotechnology*, vol. 28, no. 50, p. 504001, 2017.

[61] X. H. Yau, F. W. Low, C. S. Khe, C. W. Lai, S. K. Tiong, and N. Amin, "An investigation of the stirring duration effect on synthesized graphene oxide for dye-sensitized solar cells," *PLoS One*, vol. 15, no. 2, p. e0228322, 2020.

[62] V. H. Pham *et al.*, "Chemical functionalization of graphene sheets by solvothermal reduction of a graphene oxide suspension in N-methyl-2-pyrrolidone," *J. Mater. Chem.*, vol. 21, no. 10, pp. 3371–3377, 2011.

[63] F. T. Johra, J.-W. Lee, and W.-G. Jung, "Facile and safe graphene preparation on solution based platform," *J. Ind. Eng. Chem.*, vol. 20, no. 5, pp. 2883–2887, 2014.

Appendix A

NMR, LC MS, and FTIR spectra for compounds **2** and **4**, zeta potential for GO and rGO, and Stern-Volmer plot were provided in the supporting information file.